A Method for Unbiased High-Resolution Aerosol Retrieval from Landsat

Alexei Lyapustin

GEST Center, University of Maryland, Baltimore County, Baltimore, and NASA Goddard Space Flight Center, Greenbelt, Maryland

D. L. Williams, B. Markham, J. Irons, and B. Holben

NASA Goddard Space Flight Center, Greenbelt, Maryland

Y. Wang

GEST Center, University of Maryland, Baltimore County, Baltimore, and NASA Goddard Space Flight Center, Greenbelt, Maryland

ABSTRACT

Because the land surface reflectance varies spatially, the atmospheric radiative transfer over land in clear-sky conditions is essentially three-dimensional. This is manifested through horizontal radiative fluxes that blur satellite images. It is important that the atmospheric blurring *systematically* increases the apparent brightness of the dark pixels. As a consequence, there are systematic biases in the satellite products of aerosol optical thickness and surface albedo over dark targets based on 1D theory, which may have a negative impact on climate research. Below, a new dark target method is presented for unbiased simultaneous retrieval of the aerosol model and optical thickness over land from Landsat Enhanced Thematic Mapper Plus (ETM+) data, based on 3D radiative transfer theory. The method automatically selects an aerosol model from a large set of candidate models using a statistical approach of the probability distribution function. The dark target method of aerosol retrieval in the blue and red bands relies on prediction of the surface reflectance in these bands from the shortwave infrared region (2.1–2.2 μm) based on the linear regression. In the Moderate Resolution Imaging Spectroradiometer (MODIS) algorithm, the regression coefficients are constants, whereas different studies indicate that they have seasonal and geographic variations. The work here shows that the accuracy of aerosol retrieval over land can be significantly increased based on ancillary information on the regional and seasonal distribution of the regression coefficients. This information, which is called surface climatology, can be derived globally around Aerosol Robotic Network (AERONET) sites, using AERONET aerosol and water vapor information for accurate atmospheric correction. This paper describes the developed method in application to Landsat data and its initial validation with AERONET measurements for a set of ETM+ images of the Washington–Baltimore area, and studies biases of 1D retrievals.

1. Introduction

Presently, large uncertainties in the climate system are associated with atmospheric aerosol (Houghton et al. 2001). Anthropogenic aerosols over land are, perhaps, the least accurately quantified. The main reason is a strong spatiotemporal variability and a wide range of microphysical and optical properties of the aerosol particles (Kaufman et al. 2002, and references within). Another factor is our limited ability to remotely sense aerosols from space over land. The most accurate retrievals are made over dark dense vegetation (DDV) targets that are not uniformly available over the globe. Even where the DDV targets are available, the finest spatial resolution of the modern global observation sys-

tems is often too coarse to perform accurate aerosol retrievals over the urban/industrial regions. Here, the limiting factor is the small size of the DDV targets in the cities or zones of industry that may often vary from a few tens of meters (clumps of trees) to several hundred meters (small fields and parks). Satellite monitoring of the main sources of the man-made pollutants is important to understand the climate forcing of anthropogenic aerosols (Charlson et al. 1992). This defines a unique niche for the Landsat high-resolution measurements even though the repeat rate of such observations is low. There are other needs for the high-resolution aerosol research, such as analysis of the air quality or investigation of the possible links of aerosols to human health (e.g., rate of respiratory diseases) in the large cities that require a small-scale analysis of air pollution.

Specific to such analysis is a high inhomogeneity and contrast of surfaces, combined with the small size of

Corresponding author address: Alexei Lyapustin, NASA-GSFC, Mailcode 920, Greenbelt, MD 20771.
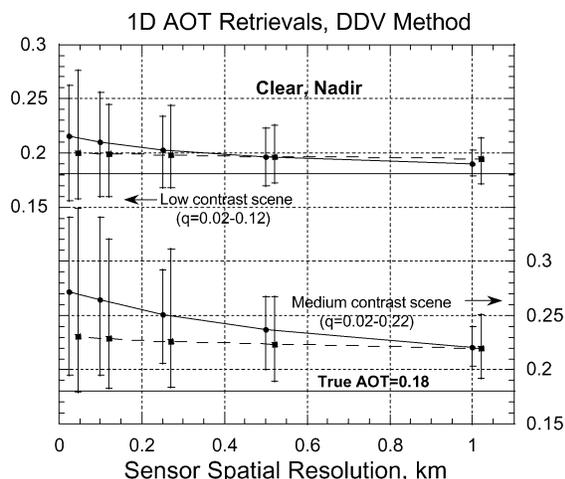E-mail: alyapust@pop900.gsfc.nasa.gov

FIG. 1. Results of aerosol optical thickness retrieval using 1D theory over dark targets as a function of sensor's spatial resolution. The true optical depth, shown by a horizontal bar, is 0.18. The upper lines (left scale) and lower lines (right scale) correspond to the surfaces of low and medium contrast. Error bars show the total range of retrieved values over a large number of pixels, and the curves give the average result. The solid and dashed lines represent two scales of surface nonhomogeneity: in the first case, the size of the uniform area varied randomly from 25 to 250 m; in the second case it varied from 25 m to 2 km.

sparsely located DDV targets. Such conditions enhance the atmospheric blurring of satellite images otherwise known as adjacency effect (Otterman and Fraser 1979). Importantly for our discussion, the blurring *systematically* increases the apparent brightness of the dark pixels that are suitable for aerosol retrieval. The conventional 1D retrieval methods ignore the atmospheric blurring, and as a result, systematically overestimate the aerosol optical thickness over land. Lyapustin and Kaufman (2001) studied errors of 1D aerosol retrievals based on the accurate simulations for surfaces of different contrasts and scales of inhomogeneity. The main result is reproduced in Fig. 1. It shows that the retrievals of aerosol optical thickness (AOT) at 30-m resolution are critically affected by the adjacency effect, and the error can exceed 100% over the surfaces of medium contrast. This error decreases with the sensor spatial resolution. However, Fig. 1 shows that the errors of 1D retrievals can be significant even at 1-km resolution for conditions of the medium or high surface contrast.

Recently, we derived a general solution to the problem of 3D atmospheric radiative transfer over spatially nonuniform anisotropic surface (Lyapustin and Knyazikhin 2001, 2002) using the Green's function technique. In the next section, the new theory will be applied to develop a method of unbiased aerosol retrieval over dark targets. The following sections 3 and 4 discuss the models of surface and aerosol used in retrievals. The last section describes results of processing six Landsat scenes, validation against Aerosol Robotic Network

(AERONET; Holben et al. 2001) measurements, and studies of the accuracy of 1D retrievals.

This work is a first important step in developing a unified frame for aerosol retrieval and atmospheric correction for the Landsat data based on 3D radiative transfer theory. At present, the implemented processing chain includes ingestion of level 1G Landsat data, radiometric calibration, generation of a mask of DDV pixels, water pixels, and dark water pixels along with the cloud mask and the aerosol retrieval. We have adopted the Landsat Automatic Cloud Cover Assessment (ACCA) cloud mask algorithm (Irish 2000).

2. Theory of 3D aerosol retrieval

For the purpose of aerosol retrieval, we will use the Lambertian approximation of the general formulas. For the Landsat application, this is justified by the fixed nadir look angle and our focus on the dark targets. Over the Lambertian surface of albedo $q(r)$, the nadir top-of-the-atmosphere (TOA) radiance can be expressed as (Lyapustin and Knyazikhin 2002)

$$L(r; \mu_0) \cong D(\mu_0) + \frac{E_0(\mu_0)}{1 - \bar{q}c_0}$$

$$\times \left[q(r)e^{-\tau} + \bar{q}\chi \right.$$

$$\left. + \frac{1}{(2\pi)^2} \int_{-\infty}^{+\infty} \frac{\tilde{q}(p)A(p)}{1 - \bar{q}c(p)} \exp(-ipr) \, dp \right],$$

(1)

where D is path radiance, $E_0(\mu_0)$ is surface irradiance created by the direct sunlight and path radiance, χ is a diffuse component of the upward atmospheric transmittance, $T = e^{-\tau} + \chi$, and c_0 is spherical albedo of the atmosphere. Below, we omit the cosine of solar zenith angle (SZA) μ_0 for brevity. In the last term of Eq. (1), which describes the diffuse transmission of the variation of the surface-reflected radiance, A is the amplitude of the diffuse atmospheric optical transfer function (OTF), $c(p)$ is spherical albedo of atmosphere at spatial frequency p, and $\tilde{q}(p)$ is spatial Fourier transform of the surface albedo variation. Formula (1) assumes that the atmosphere is laterally homogeneous, and the surface is the only source of spatial variations. Our numerical analysis shows that for most conditions, except very high surface contrast, the last term is relatively small, and can be neglected in the aerosol retrieval. Thus, we can rewrite Eq. (1) as

$$L(r) \cong D + \frac{E_0}{1 - \bar{q}c_0}[q(r)e^{-\tau} + \bar{q}\chi]. \qquad (2)$$

For the purpose of aerosol retrieval, the albedo of DDV pixel $q(r)$ in the blue and red bands can be predicted using measured reflectance in the shortwave infrared

(SWIR) band (2.1 μm) using linear regression (Kaufman et al. 1997). Having fixed the aerosol model, we have two unknowns left in Eq. (2), namely, AOT and mean surface albedo $\overline{q}$ of the area surrounding the DDV pixel in point **r**. In order to conclude the system, we add the 1D equation for the mean radiance in point **r**:

$$\overline{L} = D + \overline{q}\frac{E_0 T}{1 - \overline{q}c_0}, \qquad (3)$$

which is obtained by averaging the measurements over a large area around the given dark pixels. Introduction of parameter $\beta = (\overline{L} - D)/E_0 T$ yields an implicit equation for AOT retrieval that has a unique root:

$$L(r) \cong D + q(r)E_0 e^{-\tau}(1 + \beta c_0) + \beta E_0 \chi. \qquad (4)$$

When the surface contrast is very large (e.g., partial snow cover), the aerosol retrieval becomes an iterative procedure inseparable from the atmospheric correction. This much more complex algorithm is far beyond the scope of this paper. Our experience with Landsat data shows that formula (4) is adequate for accurate unbiased aerosol retrievals (see section 5) in snowless conditions. This formula contains only the atmospheric functions that are well known from 1D radiative transfer theory. Thus, the advantage of this algorithm is simplicity and high efficacy: it only requires an additional averaging over the moving window, as compared to the 1D algorithm, and can be implemented operationally. The size of averaging window depends on many factors including scale of surface inhomogeneity and surface contrast, the average height of aerosol layer and a typical scale of horizontal variability of aerosol, etc. Our earlier theoretical and simulation studies (Lyapustin 2001) showed that the window size of 2–5 km quite accurately represents the 1D regime over land under a variety of conditions. In this work, we are using the window of 3 km $\times$ 3 km, which was additionally adjusted by trial and error based on real Landsat scenes. Also, below, we refer to $\overline{q}$ and $\overline{L}$ as locally averaged quantities.

The traditional remote sensing of aerosol and land surface reflectance is based on the independent pixel approximation (IPA), that is, formula (3) applied on a pixel level. Comparison of IPA with the 3D solution shows a difference $[\overline{q} - q(r)][E_0 \chi/(1 - \overline{q}c_0)]$, which over the dark targets, is systematically interpreted by the 1D algorithm as an excessive AOT.

In order to account for the finite bandwidth of the Landsat spectral channels, formula (4) is rewritten as follows:

$$L(r) \cong D^{\Delta\lambda} + q(r)\langle E_0 e^{-\tau}\rangle_{\Delta\lambda}(1 + \beta^{\Delta\lambda} c_0^{\Delta\lambda}) + \beta^{\Delta\lambda}\langle E_0 \chi\rangle_{\Delta\lambda}, \qquad (5)$$

where $\beta^{\Delta\lambda} = (\overline{L} - D^{\Delta\lambda})/\langle E_0 T\rangle_{\Delta\lambda}$, and superscript $\Delta\lambda$ and brackets $\langle\,\rangle_{\Delta\lambda}$ indicate spectral averaging. For example,

$$D^{\Delta\lambda} = \frac{\int_{\Delta\lambda} \frac{F_{0\lambda}}{\pi} D_\lambda h_\lambda\, d\lambda}{\int_{\Delta\lambda} \frac{F_{0\lambda}}{\pi} h_\lambda\, d\lambda}, \qquad (6)$$

where h_λ is the spectral bandpass function of the Landsat channel, $F_{0\lambda}$ is the extraterrestrial solar flux, and the monochromatic path radiance is calculated for the unitary solar illumination.

3. Surface climatology

The AOT retrieval relies on independent evaluation of the surface reflectance (q_s^λ). In Moderate-Resolution Imaging Spectroradiometer (MODIS) blue (0.47 μm) and red (0.66 μm) bands, q_s^λ is predicted from the TOA SWIR (2.1 μm) measurements (ρ^{SWIR}) over the DDV targets (Kaufman et al. 1997) with an accuracy of 0.006 (Karnieli et al. 2001):

$$q_s^{\text{Blue}} = 0.25\rho^{\text{SWIR}}; \qquad q_s^{\text{Red}} = 0.5\rho^{\text{SWIR}}. \qquad (7)$$

This relation has a strong physical basis for vegetation due to the correlation of chlorophyll absorption in the blue and red and absorption of liquid water in the SWIR. The use of the SWIR band is very convenient as it has very little atmospheric contamination except for conditions of high aerosol loading and presence of dust. Originally, the regression coefficients of Eq. (7) were derived from a limited number of ground spectrometer measurements and Airborne Visible Infrared Imaging Spectrometer (AVIRIS) flight data. It is clear that they depend on many factors including type of vegetation, its phenophase, and stress condition, etc. These relations may have geographic and seasonal dependence. Therefore, for reliable aerosol retrievals one needs to establish a reliable surface climatology of the regression coefficients.

In this work, we performed an atmospheric correction of six available Landsat images around the AERONET site at the National Aeronautics and Space Administration (NASA) Goddard Space Flight Center (GSFC) using AERONET retrievals to characterize aerosols. For this purpose, we developed a code for the full 3D atmospheric correction of the Landsat data. In detail, this method will be described elsewhere. Here, we only mention the main steps of processing: 1) calculate the average surface albedo from the mean TOA radiance using Eq. (3); 2) make the Fourier transform ($\hat{F}$) of the radiance spatial variation [see Eq. (1)],

$$\hat{F}[L(r) - \overline{L}]\left(\frac{E_0}{1 - \overline{q}c_0}\right)^{-1} = \tilde{q}(p)\frac{e^{-\tau} + A(p)}{1 - \overline{q}c(p)}, \qquad (8)$$

and calculate the Fourier transform of the surface albedo variation $\tilde{q}(p)$; 3) find $\tilde{q}(r)$ by applying the inverse Fourier transform, and calculate surface albedo as $q(r) = \overline{q} + \tilde{q}(r)$. As before, all the RT functions used in cal-

FIG. 2. Comparison of RGB color composites of (left) measured TOA reflectance and (right) corrected surface albedo for ETM+ image of 5 Oct 2001. The R, G, and B components are equally weighted.

culations represent spectrally integrated values in order to account for the width of the Landsat spectral bands. The 3D RT functions $A(p)$ and $c(p)$ are calculated using our solution for atmospheric optical transfer function with the method of spherical harmonics (Lyapustin and Muldashev 2001). The accuracy of retrieved surface albedo given the perfect knowledge of atmospheric conditions is several relative percent, the same as the accuracy of Eq. (1).

Using this code, we performed correction of all Landsat channels for the subscenes of 512×512 pixels around GSFC. By visual imagery analysis, we select cases with homogeneous atmosphere within the radius of 7–8 km. An example of atmospheric correction of

the ETM+ image around GSFC acquired on 5 October 2001 is shown in Fig. 2.

The derived surface albedoes, which are regionally representative and have a large sampling statistics and seasonal dependence, allow us to get a better insight into the nature of regression (7). Figure 3a shows scatterplots of relation ρ_s^{Blue} versus ρ^{SWIR} and ρ_s^{Red} versus ρ^{SWIR} for the DDV pixels of the ETM+ scene of 11 May 2000 around GSFC. The DDV pixels were selected based on the criteria

$$\text{NDVI}_s \geq 0.75, \quad \text{and} \quad 0.01 \leq \rho_s^{\text{SWIR}} \leq 0.05. \quad (9)$$

The line shows the best-fit linear regression $\rho_s^\lambda = A + B\rho_s^{\text{SWIR}}$. For all processed experiments, the offset A was
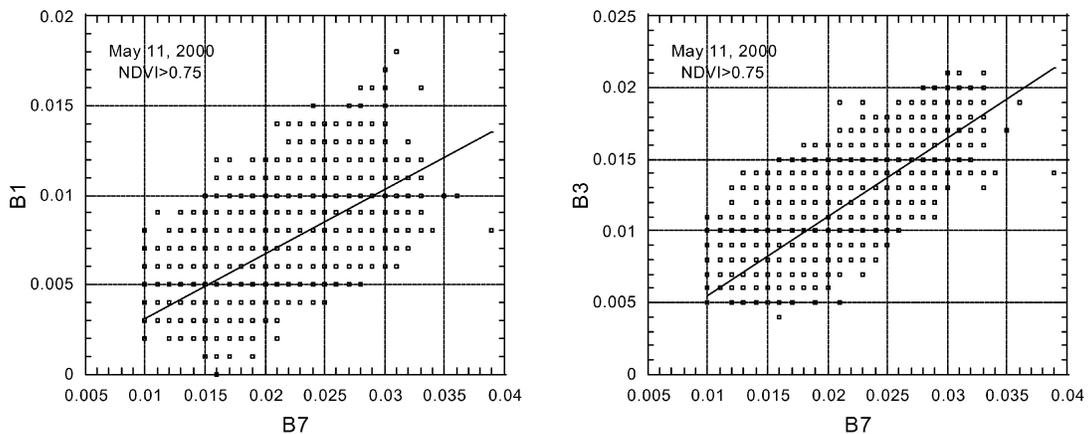
FIG. 3. The regression of surface reflectance for the DDV pixels between ETM+ band 7 (2.2 μm), band 1 (0.477 μm), and band 3 (0.66 μm).

FIG. 5. Illustration of the weight distribution for aerosol models for two different days. The model is defined by the modal radius of the fine fraction R_{vf} = (0.04, 0.07, . . . , 0.23) and the ratio of concentration C_{vc}/C_{vf} = (0, 0.1, 0.2, . . . , 8).
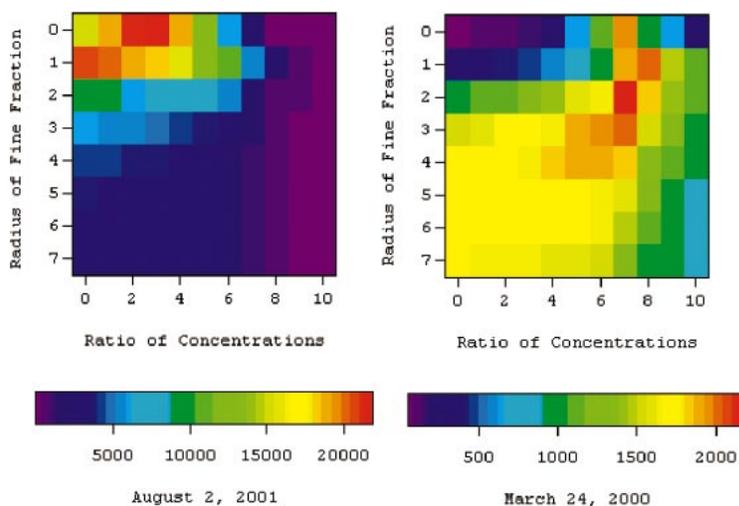
spectral dependence of AOT in ETM+ bands B1 and B3 in grid points $\tau^{0.44}$ = 0.25, 0.3, 0.35, for two aerosol models with the same fine and coarse fractions but different ratio C_{vc}/C_{vf} = 0.1 and 1. During retrievals, the algorithm goes incrementally through every combination of pairs (R_{vf}, C_{vc}/C_{vf}). The pair is considered to be a candidate solution, if the retrieved $\tau^{0.477}$ and $\tau^{0.66}$ reside within the same AOT bin (e.g., $\tau_i^{0.44}$ = 0.25, $\tau_{i+1}^{0.44}$ = 0.3), and occupy the same relative position within the bin. Thus, in the absence of noise, the best candidate is the model that provides the smallest "bin travel" distance.

In reality, there are always systematic and random AOT retrieval errors related to the earlier-discussed uncertainties of the surface reflectance. For this work, we eliminated systematic errors provided that the local surface estimates around the GSFC AERONET site are representative of the whole image ($\approx$180 km). Still, there are random retrieval errors due to uncertainty of predicting surface reflectance (δ = $\pm$0.005–0.009). These errors are uncorrelated in the blue and red bands. There are two consequences of this fact: 1) more accurate retrieval would require accumulation of the retrieval statistics over a number of DDV pixels, and 2) aerosol models with nonzero bin-travel distance may also be a solution. In order to discriminate between different potential solutions, we divided each $\Delta\tau^{0.44}$ bin into five subbins and defined the integer "travel" distance (y) as the difference in the subbin number between retrieved AOT $\tau^{0.477}$ and $\tau^{0.66}$. Based on that, we introduced weights (w) for different travel distances $w = a^y$, where $a < 1$. The weight is designed to reward the perfect model ($y = 0$) and punish imperfect ones ($y > 0$) still considering them as potential solutions. Each of 88 models is evaluated for the whole image by summing weights for every retrieval. Figure 5 shows two examples of obtained distributions, which are essentially

probability distribution functions of different aerosol models given the uncertainties of surface reflectance. From these distributions, we finally derive the most probable modal radius and ratio C_{vc}/C_{vf} that define the dominant aerosol model. The value of base a in weight calculation is selected according to the discretization of $\Delta\tau^{0.44}$ grid (the number of subbins) and the uncertainty in the surface reflectance (δ). We found that the use of base a = 0.3–0.5 gives stable selection of the dominant aerosol model.

The final aerosol optical thickness is then retrieved with the dominant model. Here, in order to additionally reduce the role of spectrally uncorrelated surface reflectance errors, we make one simultaneous retrieval for a pair of measurements in the blue and red bands, since the spectral behavior of extinction had been fixed by the dominant model. As a result, we get the same average optical thickness as with the independent retrievals of AOT, but avoid unphysical spectrally uncorrelated fluctuations of AOT for the nearby pixels. This approach significantly improves spectral stability of the subsequent atmospheric correction over the dark vegetation.

The LUT generated for aerosol retrievals consists of the following functions: $\{D^{\Delta\lambda}(\mu_0), \langle E_0(\mu_0)T\rangle_{\Delta\lambda},$ $\langle E_0(\mu_0)\chi\rangle_{\Delta\lambda}, \tau^{\Delta\lambda}, c_0^{\Delta\lambda}\}$. The spectral integration uses 10 monochromatic calculations across each ETM+ band for spline interpolation in the nodes of the bandpass function. The LUT has the following dimensions: 41 values of SZA, cos(SZA) = {0.2, 0.22, . . . , 0.98, 1}, 16 AOT values specified at 0.44 μm, and 88 aerosol models for the static family. The LUT functions are linearly interpolated in SZA and AOT. In order to account for the surface height variation, we generate two LUTs, for the sea level and for the surface height of 3 km. During retrievals, we perform interpolation according to the pixel surface pressure, obtained from the Global 30-Arc-Second Elevation Data Set (GTOPO30)
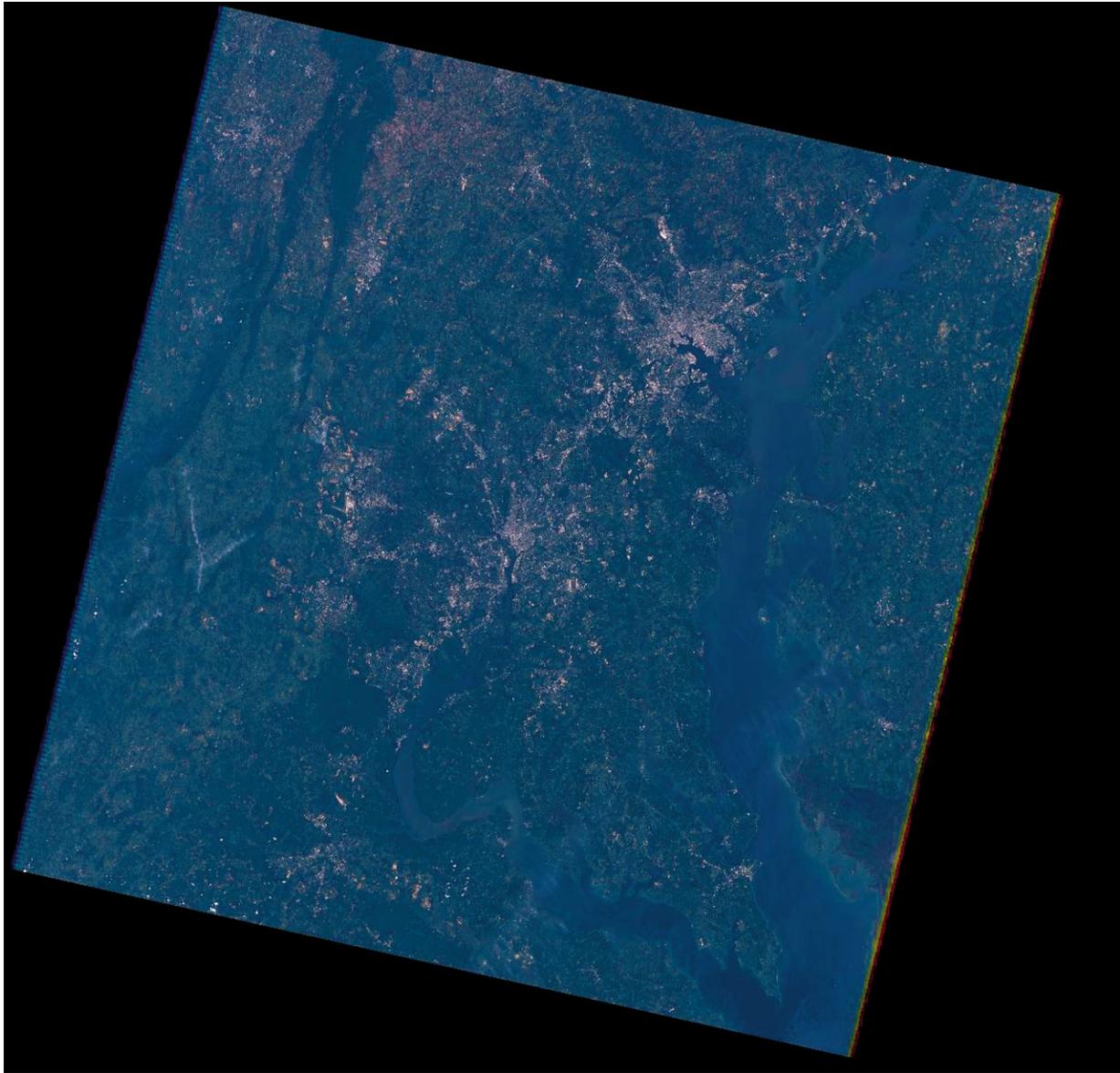
FIG. 6. The RGB color composite of the ETM+ image of the Chesapeake Bay region acquired 2 Aug 2001. Washington, D.C., is in the middle, and Baltimore lies to the north. The Shenandoah Valley is on the left.

data elevation model and pressure profile from the relevant Standard Model of Atmosphere (Berk et al. 1989). Although the described LUT generation task seems formidable, the automated procedure we developed based on the spherical harmonics (SHARM) code (Muldashev et al. 1999) is very fast: it only takes about 1–1.5 h on the laptop Dell Inspiron 8000 with 512-MB RAM and a 750-MHz processor to perform the full described set of calculations with an accuracy of about 0.05%. This important advantage allowed us to run a large number of test cases in order to optimize the retrieval algorithm in terms of aerosol models.

5. Results

a. Accuracy of 3D algorithm

The described method was applied to six ETM+ scenes of the Chesapeake Bay area (path 15, row 33), which have low cloud cover (0%–15%). Below, we give a detailed description for one case of 2 August 2001 followed by the discussion of AERONET validation for the other experiments.

The RGB color composite of the ETM+ image of 2 August 2001 is shown in Fig. 6. The conditions are clear with little contamination by relatively thin cirrus
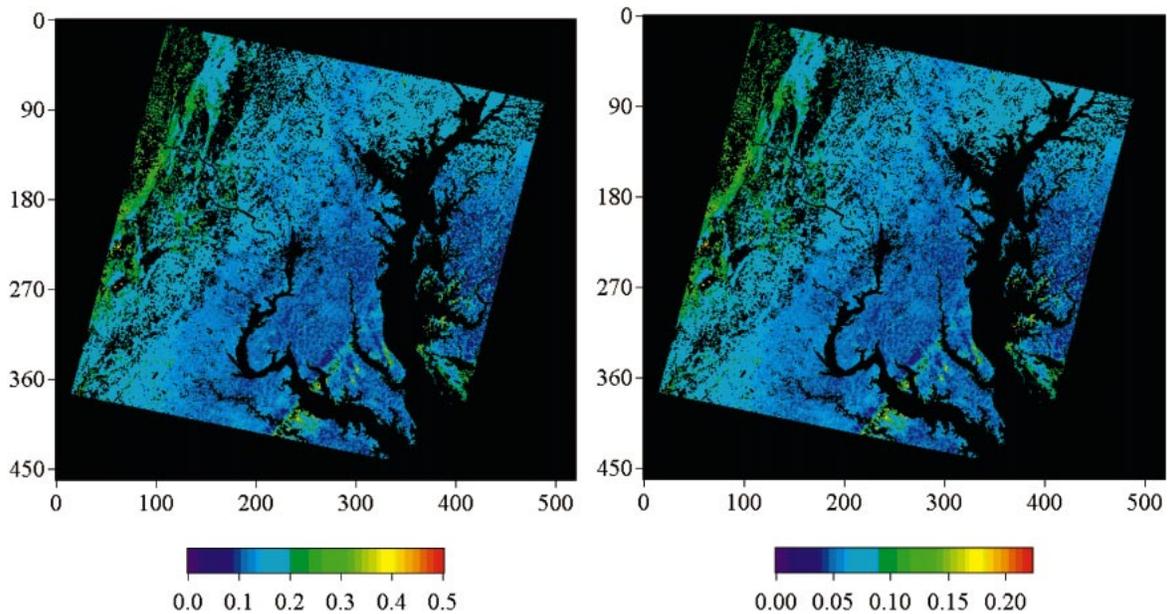
FIG. 7. AOT retrieved with the 3D algorithm in ETM+ (left) band 1 and (right) band 3 on 2 Aug 2001. The images are correlated, which is a consequence of our combined AOT retrieval in the blue and red bands with the dominant aerosol model.

clouds in the form of contrails stretching across the Potomac River and Chesapeake Bay in the northeast direction. There are also some clouds along the Shenandoah Valley (on the west) that are well seen on the thermal image. An enhanced blurring along the left side of the image, which is noticeable at the Landsat resolution of 30 m, can be identified as higher aerosol loading.

In retrievals, we applied the surface regression coefficients derived around the GSFC AERONET site (Table 1) to the whole image. The probability distribution of aerosol models for this day (see Fig. 5) yields $R_{vf} = 0.07\ \mu m$, $C_{vc}/C_{vf} = 0.2$ for the dominant model. The aerosols were retrieved at an effective ≈ 500 m resolution (16 by 16 pixels). The local average radiance required by the 3D algorithm to evaluate the mean surface albedo was calculated using the window of 3 km by 3 km.

The spatial distribution of derived AOT is shown in Fig. 7. One can see a very good qualitative agreement of the retrievals with visual imagery analysis. The aerosols have a smooth spatial distribution with an increase in the westward direction. Importantly, there is no significant aerosol variability between the high-contrast urban–industrial regions (e.g., Washington, D.C., Baltimore) and rather homogeneous vegetated areas around, which is an indirect proof of the good performance of the new algorithm. Further, we compared retrievals with available AERONET measurements at GSFC, Baltimore, and Annapolis (Fig. 8). The derived 3D AOT shown by squares are averaged over the 5 km by 5 km box centered on AERONET locations, and error bars show the one-sigma variation. The relatively large size

of the box allows us to always have at least one retrieval for comparison, especially in early spring and late fall, when the DDV targets are sparse. This is also true for the Baltimore instrument located downtown, with the closest DDV targets suitable for retrieval 1–2.5 km away. The direct sun photometer measurements of the optical thickness were typically within 15 min from satellite overpass, and the full AERONET retrievals are available within 16–35 min, except for 28 July 1999 (4 h). Figure 8 shows that for all of the processed experiments the results of the 3D algorithm are in excellent agreement with the sun photometer measurements, within ±(0.02–0.03). This agreement itself proves a robust selection of the dominant aerosol model. On the whole, our retrievals also correctly reproduce the spatial distribution of aerosol between two or three validation points. The microphysical characteristics of the selected dominant model are compared with full AERONET inversions (Dubovik and King 2000) in Table 2. Probably because very limited statistics are available and conditions are rather similar, there is no obvious correlation between these datasets. For example, both retrievals gave the lowest amount of coarse fraction for two summer cases of 28 July 1999 and 2 August 2001, yet cases of the high ratio C_{vc}/C_{vf} are not correlated. There may be two factors smearing the picture. First, our aerosol model selection is based on the whole Landsat image rather than on the local conditions. Second, AERONET and satellite retrievals use measurements in different hemispheres of the light scattering that may not necessarily carry the same information about the aerosol microphysics. Also, only two bands of spectral information are available for our retrievals, while AERONET
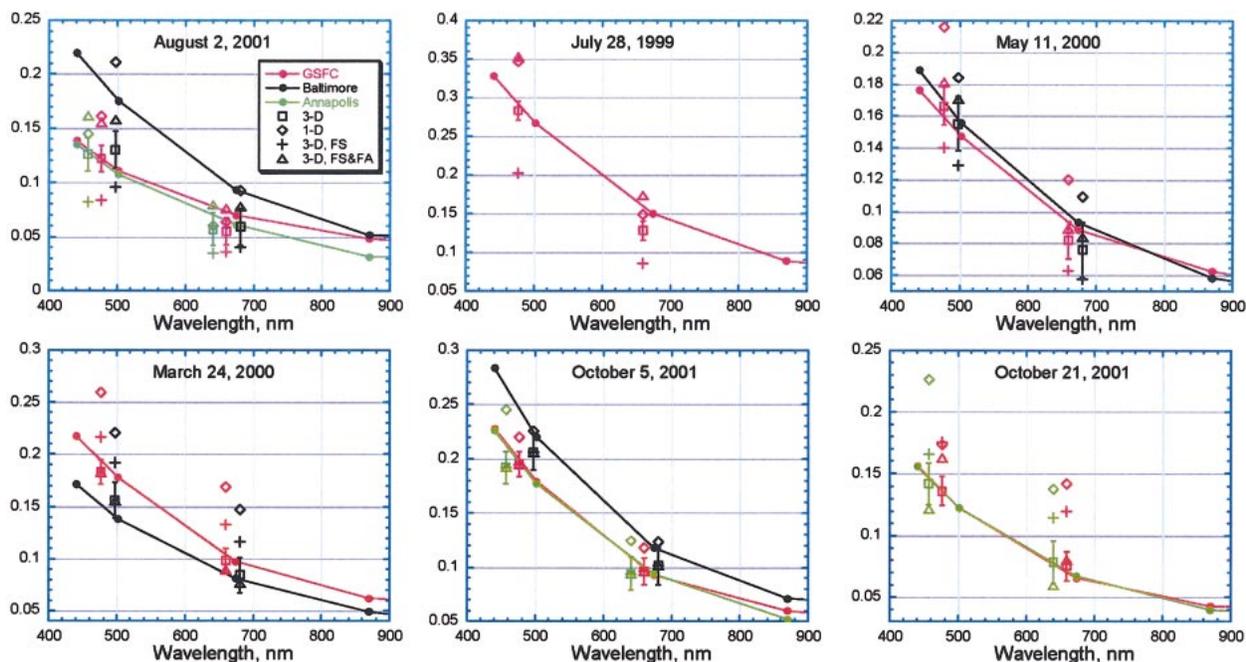
FIG. 8. Comparison of ETM+ retrievals with AERONET measurements. Filled circles connected by lines show the sun photometer measurements in GSFC (red), Baltimore (black), and Annapolis (green). The same color coding applies to ETM+ retrievals for bands 1 and 3, where □ and ◇ show the results of 3D and 1D algorithm, respectively. For the visualization purpose, the results for Annapolis and Baltimore are shifted 20 nm to the left and right from the respective ETM+ bands. Also shown are two additional 3D retrievals. The fixed surface regression coefficients (0.35, 0.55) are indicated by (+), FS; (△) indicates retrievals with fixed regression coefficients and fixed aerosol model, FS & FA.

uses six-band spectral and multiangular information at additional constraints by the direct measurements of the optical thickness. Given all that, we consider it very encouraging that the range of derived $(R_{vf}, C_{vc}/C_{vf})$ values is very similar to the AERONET results. We hope that with accumulation of the retrieval statistics, we will soon be able to ascertain the usability of the developed method for characterization of the aerosol properties in terms of a combination of radius of fine mode and ratio of concentrations.

The demonstrated high accuracy of AOT retrievals requires a considerable effort on development of surface climatology (regionally and seasonally dependent regression coefficients) and time-consuming retrievals for a large set of candidate aerosol models. On the other hand, the MODIS land aerosol algorithm uses constant regression coefficients for the whole globe, and several

discrete aerosol models for the main aerosol types. We conducted an additional study trying to answer the following two questions. What accuracy of AOT retrieval do we get in the MODIS-like approach with 1) surface regression coefficients fixed at the average level (0.35, 0.55), and 2) additionally fixed aerosol model (R_{vf} = 0.1 μm, C_{vc}/C_{vf} = 0.3)? The corresponding retrievals are shown in Fig. 8 with (+) and (Δ), respectively. One can see the deterioration in accuracy by a factor of 3–5 for five out of six experiments with fixed regression coefficients (the case of 5 October 2001 should not be considered because the fixed parameters coincide with the accurate results). When we additionally fixed the aerosol model using the average parameters, the retrieval results even slightly improved. This tells us that fixing the regression coefficients, even at the regional level, introduces error so large that the selection of aerosol

TABLE 2. Comparison of the aerosol microphysical properties derived from ETM+ data with AERONET retrievals. Columns 2–4 give the AERONET values for radii of the fine and coarse modes, and ratio of concentrations for GSFC, Baltimore, and Annapolis, respectively. The last two columns show the radius of fine mode and the concentration ratio of the dominant aerosol model.

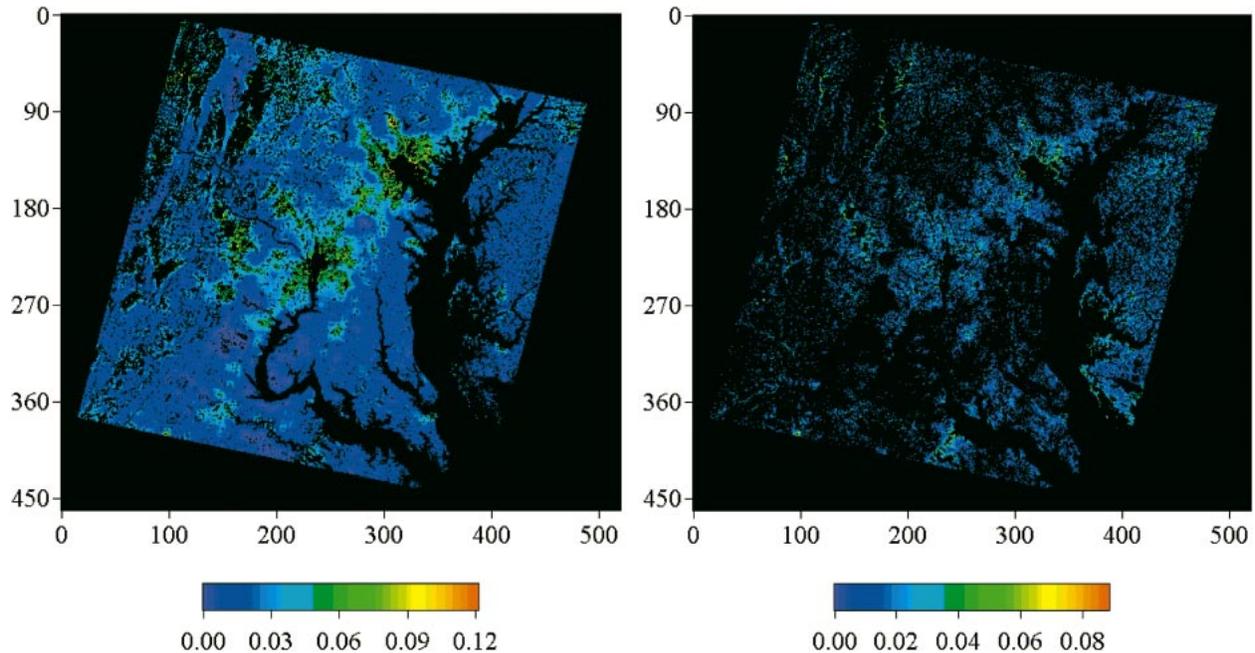| Date	R_{vf}	R_{vc}	C_{vc}/C_{vf}	R_{vf}	C_{vc}/C_{vf}
28 Jul 1999	0.146	3.24	0.44	0.1	0.3
24 Mar 2000	0.146, 0.127	2.63, 2.86	0.51, 0.48	0.15	0.75
11 May 2000	0.153, 0.165	2.21, 2.58	1.03, 1.5	0.125	0.5
2 Aug 2001	0.148, 0.136, 0.098	3.77, 3.28, 2.95	0.92, 0.35, 0.28	0.07	0.2
5 Oct 2001	0.142, 0.136, 0.137	3.1, 3.62, 3.44	0.83, 0.97, 0.58	0.125	0.5
21 Oct 2001	0.136, 0.127	2.92, 3.19	0.91, 0.43	0.15	1.0

FIG. 9. The difference in aerosol optical thickness retrieved with 1D and 3D algorithms. Results for ETM+ (left) band 1 and (right) band 3, respectively.

model becomes unstable, so the additional constraining of the aerosol model stabilizes somewhat the AOT retrieval. This conclusion shows a pathway to a considerable improvement in aerosol retrievals through the development of geographically and seasonally representative surface climatology around AERONET sites. We have initiated this work and plan to continue using ETM+ measurements collected by the MODIS land validation group. In parallel, we are developing the rigorous algorithm of the full atmospheric correction of MODIS data using ancillary information on aerosol and water vapor from AERONET and National Centers for Environmental Prediction (NCEP) ozone data. This work will provide a basis for potentially significant improvement of the operational aerosol retrievals over land.

b. AOT biases

In order to evaluate biases of the 1D algorithm predicted by theory (Fig. 1), we have also performed 1D AOT retrievals using the dominant aerosol model selected by the 3D algorithm. The corresponding results over the AERONET sites are shown by diamonds in Fig. 8. One can see that, in agreement with theoretical predictions, there is a nonnegligible positive bias caused by the land surface inhomogeneity. As we mentioned earlier, the shown data are averaged over the 5-km window. The analysis of the individual retrievals shows a larger variation of 1D AOT as compared to 3D AOT.

Assuming 3D retrievals as a truth, we can now look at the spatial distribution of the error of the traditional 1D algorithm shown for 2 August 2001 in Fig. 9. In general, over the relatively homogeneous vegetated areas the difference between 1D and 3D results in clear conditions is relatively small, within 0.02 in the blue and 0.01 in the red. However, the error sharply increases and reaches 100% and more over the urban centers, where the surface brightness and contrasts are higher.

For comparison, Fig. 10 shows 1D MODIS aerosol product (MOD04) for 2 August 2001. The MODIS algorithm uses measurements at 500-m resolution at nadir, and makes retrievals at an aggregated 10-km scale. One can see a factor of 1.5–3 higher amount of the retrieved aerosol over Baltimore and Washington, D.C., as compared to the background level, and 2–4 times larger AOT in comparison to AERONET measurements. The 3D radiation effects discussed above have, probably, a minor role in these errors. The main reason for these artifacts is that in the current MODIS algorithm the surface regression technique (7) is not limited to the DDV targets but extends to much brighter surfaces (Kaufman et al. 1997). Our analysis of the atmospherically corrected ETM+ data shows that, in this case, the uncertainty of regression grows by a factor of 2–6, and importantly, the slope of regression shifts from the average 0.35/0.55 in the blue/red to the higher values ($\approx$0.7–1.2). If this increase in the slope is not a priori taken into account in the algorithm, then the retrieved AOT becomes correlated with the surface brightness, which is what we see in the MODIS data. This discussion shows that the current MODIS aerosol product over large cities and industrial centers should be used with extreme caution in aerosol and climate studies, as these data may be seriously biased.
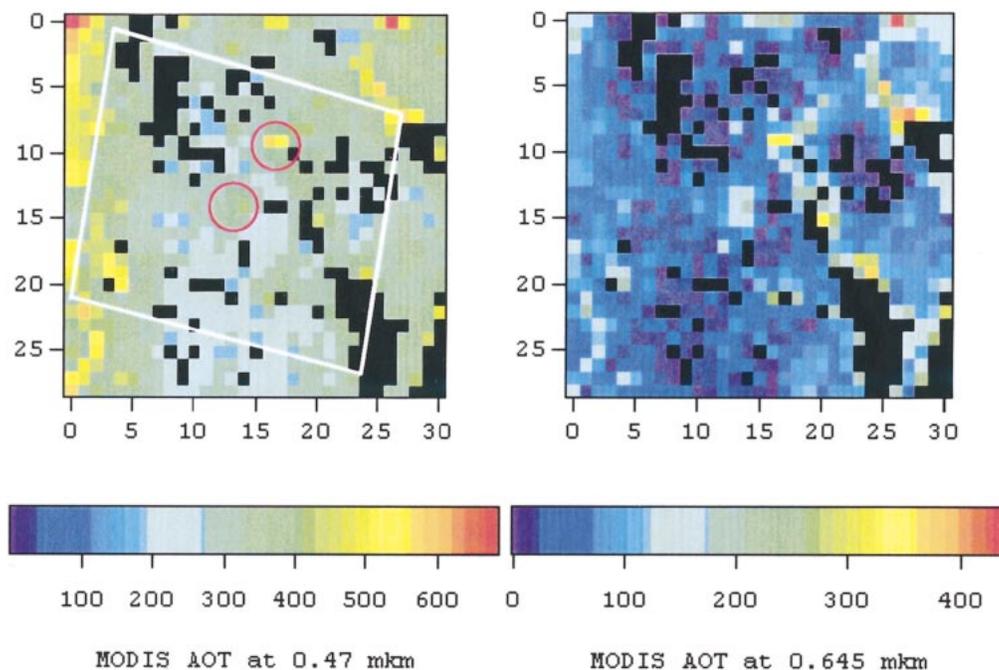
FIG. 10. The MODIS AOT product for 2 Aug 2001 (scaling factor is 1000). The white lines in the left image show approximately the boundaries of the ETM+ image. Two red circles show the locations of Baltimore and Washington, D.C.

6. Conclusions

In this paper we described a new dark target method of aerosol retrievals over land. The new method is based on 3D radiative transfer theory that removes positive biases of 1D retrievals when the surface is nonhomogeneous. The method is designed to simultaneously retrieve the aerosol model described by the bimodal distribution, and optical thickness. The model of aerosol is selected from the representative family of models, which is quasi continuous in the radius of fine fraction and in the ratio of concentrations of the coarse and fine fractions. We fixed the refractive indices of aerosol particles based on average AERONET values for the region. The best-fit aerosol model is selected based on the probability distribution function calculated from the image for the whole space of the candidate models. The way to build this space is not unique, but is logical and optimized by trial and error. Remer and Kaufman (1998) recently introduced the concept of dynamic aerosol model in which the particles grow and other parameters may change with aerosol loading. Later, Dubovik et al. (2002) summarized a large statistics of AERONET retrievals to describe the dynamic models for different worldwide locations. The static model we used in this research does not preclude solution from dynamic behavior, which would be selection of the larger radius of the fine fraction at higher aerosol loading. On the other hand, since dynamic growth of aerosol particles is not observed everywhere (O. Dubovik 2003, personal communication), our static model does not force the solution

to behave "dynamically." At present, the static family of models is tuned to the meteorological conditions of the Baltimore–Washington, D.C., region. With geographical broadening of the new method's application, we will develop complementary models based on growing AERONET statistics for the main aerosol types.

A validation of the six processed ETM+ scenes with measurements of three AERONET stations showed an excellent accuracy of the retrieved aerosol optical thickness ($\pm$0.02–0.03). The observed very high accuracy is probably a result of several factors that favored our study. First, the estimate of accuracy is based on a very limited number of processed cases (six), and is not statistically representative. Second, the atmospheric conditions were stable in all cases, with, probably, the same dominant aerosol type that is described well by the GSFC Urban-Industrial Model (Dubovik et al. 2002), and, which, in turn, we used to build a static family of aerosol models used in retrievals. For example, change of air masses bringing different types of smoke or dust into the region would definitely lower the overall accuracy. For all of these reasons, we do not consider the obtained accuracy ($\pm$0.02–0.03) as a representative characteristic of the new method, rather as an objective that may be achievable on the regional level under the dominant and stable atmospheric conditions.

The accuracy of the new algorithm does not deteriorate over the brighter and high-contrast urban–industrial regions, which is a significant drawback of 1D methods. In combination with the high-resolution of

Landsat, which catches small patches of vegetation in the urban developments, large cities and industrial centers, the new method may become a very important tool for studying the sources of the man-made pollutions. In the near future, we are planning to test the sensitivity of the new method to detect variability of aerosols over large cities from Landsat, which is very important for the air quality control and environmental and health issues.

One important conclusion of our study is the need for development of the regionally tuned surface climatology. Such ancillary information derived worldwide around AERONET sites will lead to significant improvement of the accuracy of operational aerosol retrievals over land. As we showed in section 3, on the regional level the regression coefficients have an expected and nonnegligible seasonal dependence, at least in northern latitudes. Thus, removal of seasonal trends in the aerosol data will be invaluable for an improved atmospheric correction. In particular, this alone will improve reliability of the time series analysis of vegetation, which is one of the important methods of climate analysis.

REFERENCES

Berk, A., L. S. Bernstein, and D. C. Robertson, 1989: MODTRAN: A moderate resolution model for LOWTRAN 7. Air Force Geophysics Laboratory Tech. Rep. GL-TR-89-0122, 256 pp.

Charlson, R. J., 1992: Climate forcing of anthropogenic aerosols. *Science,* **255,** 423–430.

Dubovik, O., and M. D. King, 2000: A flexible inversion algorithm for retrieval of aerosol optical properties from Sun and sky radiance measurements. *J. Geophys. Res.,* **105,** 20 673–20 696.

——, B. Holben, T. F. Eck, A. Smirnov, Y. J. Kaufman, M. D. King, D. Tanre, and I. Slutzker, 2002: Variability of absorption and optical properties of key aerosol types observed in worldwide locations. *J. Atmos. Sci.,* **59,** 590–608.

Holben, B., and Coauthors, 2001: An emerging ground-based aerosol climatology: Aerosol optical depth from AERONET. *J. Geophys. Res.,* **106,** 9807–9826.

Houghton, J. T., Y. Ding, D. J. Griggs, M. Nogver, P. J. van der Linden, X. Dai, K. Maskell, and C. A. Johnson, 2001: *Climate Change 2001—The Scientific Basis.* Cambridge University Press, 881 pp.

Irish, R., 2000: *Landsat 7* automatic cloud cover assessment. Algorithms for multispectral, hyperspectral, and ultraspectral imagery. *Proc. SPIE,* **4049,** 348–355.

Karnieli, A., Y. J. Kaufman, L. Remer, and A. Wald, 2001: AFRI—Aerosol free vegetation index. *Remote Sens. Environ.,* **77,** 10–21.

Kaufman, Y. J., D. Tanre, L. A. Remer, E. F. Vermote, A. Chu, and B. N. Holben, 1997: Operational remote sensing of tropospheric aerosol over land from EOS moderate resolution imaging spectroradiometer. *J. Geophys. Res.,* **102,** 17 051–17 067.

——, ——, and O. Boucher, 2002: A satellite view of aerosols in the climate system. *Nature,* **419,** 215–223.

Lyapustin, A. I., 2001: 3-D effects in the remote sensing of surface albedo. *IEEE Trans. Geosci. Remote Sens.,* **39,** 254–263.

——, and Y. J. Kaufman, 2001: Role of adjacency effect in the remote sensing of aerosol. *J. Geophys. Res.,* **106,** 11 909–11 916.

——, and Yu. Knyazikhin, 2001: Green's function method in the radiative transfer problem. I: Homogeneous non-Lambertian surface. *Appl. Opt.,* **40,** 3495–3501.

——, and T. Z. Muldashev, 2001: Solution for atmospheric optical transfer function using spherical harmonics method. *J. Quant. Spectrosc. Radiat. Transfer,* **68,** 43–56.

——, and Yu. Knyazikhin, 2002: Green's function method in the radiative transfer problem. II: Spatially heterogeneous anisotropic surface. *Appl. Opt.,* **41,** 5600–5606.

Mishchenko, M., J. E. Penner, D. Anderson, 2002: Global Aerosol Climatology Project. *J. Atmos. Sci.,* **59,** 249.

Morisette, J. T., J. L. Privette, and C. O. Justice, 2002: A framework for the validation of MODIS land products. *Remote Sens. Environ.,* **83,** 77–96.

Muldashev, T. Z., A. I. Lyapustin, and U. M. Sultangazin, 1999: Spherical harmonics method in the problem of radiative transfer in the atmosphere–surface system. *J. Quant. Spectrosc. Radiat. Transfer,* **60,** 393–404.

Otterman, J., and R. S. Fraser, 1979: Adjacency effects on imaging by surface reflection and atmospheric scattering: Cross radiance to zenith. *Appl. Opt.,* **18,** 2852–2860.

Remer, L., and Y. J. Kaufman, 1998: Dynamic aerosol model: Urban/industrial aerosol. *J. Geophys. Res.,* **103,** 13 859–13 871.

——, A. E. Wald, and Y. J. Kaufman, 2001: Angular and seasonal variation of spectral surface reflectance ratios: Implications for the remote sensing of aerosol over land. *IEEE Trans. Geosci. Remote Sens.,* **39,** 275–283.